

# Using Nearest Neighbors for Accurate Estimation of Ultrasonic Attenuation in the Spectral Domain

Md. Kamrul Hasan, Mohammad Arafat Hussain, Sharmin R. Ara, Soo Yeol Lee, and S. Kaisar Alam

**Abstract**—Attenuation is a key diagnostic parameter of tissue pathology change and thus may play a vital role in the quantitative discrimination of malignant and benign tumors in soft tissue. In this paper, two novel techniques are proposed for estimating the average ultrasonic attenuation in soft tissue using the spectral domain weighted nearest neighbor method. Because the attenuation coefficient of soft tissues can be considered to be a continuous function in a small neighborhood, we directly estimate an average value of it from the slope of the regression line fitted to the 1) modified average midband fit value and 2) the average center frequency shift along the depth. To calculate the average midband fit value, an average regression line computed from the exponentially weighted short-time Fourier transform (STFT) of the neighboring 1-D signal blocks, in the axial and lateral directions, is fitted over the usable bandwidth of the normalized power spectrum. The average center frequency downshift is computed from the maximization of a cost function defined from the normalized spectral cross-correlation (NSCC) of exponentially weighted nearest neighbors in both directions. Different from the large spatial signal-block-based spectral stability approach, a cost-function-based approach incorporating NSCC functions of neighboring 1-D signal blocks is introduced. This paves the way for using comparatively smaller spatial area along the lateral direction, a necessity for producing more realistic attenuation estimates for heterogeneous tissue. For accurate estimation of the attenuation coefficient, we also adopt a reference-phantom-based diffraction-correction technique for both methods. The proposed attenuation estimation algorithm demonstrates better performance than other reported techniques in the tissue-mimicking phantom and the *in vivo* breast data analysis.

## I. INTRODUCTION

**B**ECAUSE of the strong correlation between the attenuation coefficient (AC) and various diseases in soft tissue, measurement of attenuation by using the ultrasound pulse-echo system is emerging as a promising technology to characterize different pathological states of soft tissue *in vivo* [1]–[5]. With the assumption of constant sound

speed, typical B-mode images display the envelope information of the ultrasound echo, where time-gain compensation (TGC) is adjusted to compensate the pulse attenuation with respect to depth. After TGC correction, further shadowing (or enhancement) artifacts below the regions of higher attenuation (or lower attenuation), indicates substantial pathological changes in tissue. Using the tissue attenuation phenomenon in B-mode display, abnormal pathological changes can be detected, for example, in the liver [3], thyroid [4], prostate [5], and breast [6]. Typically, the AC is found to be low for fatty tissue and medullary carcinoma and high for fibrosis and infiltrating ductal carcinoma [7], [8] in breast tissue. Despite its significant importance for noninvasive clinical diagnosis of tissue pathology changes, no reliable technique exists in the literature, and thus it is still an open problem in ultrasound research.

The attenuation estimation methods that have been developed so far can be categorized broadly into time- and frequency-domain techniques. A limited number of time-domain attenuation estimation methods exists in the literature that exploit the zero-crossing density of the RF signal [9], entropy difference between two successive narrowband echo segments [10], and analysis of the B-mode images [11] to estimate the local AC. However, compensation for the diffraction effect in the RF echo to estimate AC accurately is very difficult for the time-domain attenuation estimation methods.

Because of linear frequency dependence of the ultrasound attenuation [9], [12], frequency-domain methods are more suited to model the attenuation phenomena in soft tissue. Two basic techniques for acoustic attenuation estimation in the frequency domain are based on spectral shift and spectral difference measurements along the axial direction. Some spectral shift methods are parametric approaches that assume a Gaussian shape of the ultrasound transmit pulse and echo, and the local AC is estimated from the slope of the linear-regression line that locally fits the center frequency downshift with respect to depth [9], [13]–[15]. In [16], power spectral cross-correlation is used to estimate the center frequency downshift with respect to depth. These spectral shift methods face challenges to minimize the diffraction effects, especially in clinical settings, resulting from the focusing of the array transducer [17]. To minimize the diffraction effects in attenuation estimation, several spectral difference methods have been developed [18]–[23]. A tissue-mimicking phantom (TMP) of known attenuation properties is used as a reference and

Manuscript received January 17, 2013; accepted March 17, 2013. This work has been supported by the Higher Education Quality Enhancement Project, University Grants Commission (CP#96/BUET/Win-2/ST(EEE)/2010), Bangladesh, and in part by the National Research Foundation of Korea grant, funded by the Korean government (2009-0078310).

M. K. Hasan, M. A. Hussain, and S. R. Ara are with the Department of Electrical and Electronic Engineering, Bangladesh University of Engineering and Technology, Dhaka, Bangladesh (e-mail: khasan@eee.buet.ac.bd).

M. K. Hasan and S. Y. Lee are with the Department of Biomedical Engineering, Kyung Hee University, Kyungki, Korea.

S. K. Alam is with Riverside Research, New York, NY.

DOI <http://dx.doi.org/10.1109/TUFFC.2013.2673>

the power spectrum of the sample tissue is normalized by the power spectrum of the reference TMP at the same depth. For this diffraction compensation technique, the settings of all the parameters must be kept the same while acquiring the sample and reference RF data. In [18] and [19], AC is estimated as a function of frequency by measuring the decay of the power spectral frequency components with respect to depth. Some other spectral difference methods estimate the local AC from the slope of the straight line that fits the log-ratio of the power spectra from the proximal and distal segments of the ROI [20]–[23], and these spectral difference methods are classified as the spectral-log difference methods. All of the spectral difference methods fail in estimating the AC properly in the lesion boundary because of the backscatter variation, although the spectral shift methods are fairly successful in this case. A hybrid method proposed in [24] combines the spectral difference and spectral shift methods to exploit the advantages of both. However, all of the spectral shift, spectral difference, and hybrid methods use a large spatial signal block to generate a stable block power spectrum, but it is often an unrealistic approach because the tissue pathology inside a large spatial region must be considered uniform, a requirement that is too idealistic for a heterogeneous tissue medium.

In this paper, we propose two novel spectral domain techniques for average ultrasonic attenuation estimation: 1) the spectral normalization-based average attenuation estimation (SNAAE), and 2) the spectral cross-correlation-based average attenuation estimation (SCAAE). Based on the assumption that a heterogeneous tissue can be modeled with several small homogeneous sub-regions [25], the local AC of a heterogeneous soft tissue can be considered pretty similar in a small subregion. Assuming that each homogeneous subregion consists of a few scan-lines, we devised our proposed techniques in such a way that an average AC for each investigating block on a particular scan-line can be estimated by using its neighborhood blocks in the axial and lateral directions. In the SNAAE method, the local AC can be estimated by using some spectral parameters, e.g., midband fit, spectral slope, and intercept, measured from the regression line that fits a system-effects-corrected power spectrum [34]. The SCAAE method, on the other hand, is based on the concept that the local AC is proportional to the derivative of the center frequency downshift with respect to depth. Here, we directly estimate an average value of AC from the slope of the regression line fitted to 1) the modified average midband fit value and 2) the average center frequency shift along depth for the SNAAE and SCAAE methods, respectively. The performance of these algorithms is evaluated using an experimental phantom as well as *in vivo* breast data and compared with other well-known attenuation estimation algorithms.

The paper is organized as follows: Section II describes the proposed SNAAE and SCAAE techniques; Section III presents the simulation and experimental results to demonstrate the strength of the proposed algorithms in

comparison to some other techniques in the literature; and conclusions are presented in Section IV.

## II. METHODS

### A. The Signal Model

Generally, ultrasound pulse–echo attenuation estimators assume a constant sound speed, linear frequency dependence of the attenuation, and homogeneous backscatters in the ROI. According to the Born approximation, multiple scattering can be ignored based on low scattering in tissues. Based on these assumptions, the received backscattered RF signal intensity  $F(f, z)$  at the transducer face can be expressed in the frequency domain as [26]

$$F(f, z) = T(f) \cdot D(f, z) \cdot A(f, z) \cdot R(f, z), \quad (1)$$

where  $T(f)$  is the transmit pulse;  $D(f, z)$  is the effect of diffraction;  $A(f, z)$  is the cumulative attenuation in the soft tissue;  $R(f, z)$  is the consequence of the scattering properties of tissue, including the effective scatter size, scatter number density, and mean square variation in acoustic impedance between the scatterers and background; and  $z$  is the depth of the ROI from the transducer face.

The transmit pulse  $T(f)$  can be assumed to be Gaussian, and it is shown with rms error analysis in [16] that the approximation error is within 10% with respect to the practical scenario. Thus, the transmit pulse can be defined as [16]

$$T(f) = e^{-(f-f_c)^2/(2\sigma^2)}, \quad (2)$$

where  $f_c$  is the center frequency and  $\sigma$  is the standard deviation of the transmit pulse. Diffraction [ $D(f, z)$ ] has the effect of distorting the spectral properties of the RF echo in the pre- and post-focal regions because of acoustic focusing of a linear-array transducer around the ROI [27]. The cumulative attenuation  $A(f, z)$  in soft tissue is a function of frequency  $f$  and depth  $z$ , and can be expressed as [12]

$$A(f, z) = e^{-4\rho(f)z} = 10^{-2\rho(f)z/86.86}, \quad (3)$$

where  $\rho(f)$  denotes the AC in nepers per centimeter. It is reported in [12] that  $\rho(f)$  demonstrates a linear frequency dependence. Therefore, it can be written as  $\rho(f) = \beta \cdot f$ , where  $\beta$  denotes the AC in nepers per centimeter per megahertz.

Soft tissue typically contains a large number of random scatters, and therefore  $R(f, z)$  can be modeled as a stochastic process [28], [29]. However, frequency dependence of  $R(f, z)$  can be modeled with power of frequency. Thus,  $R(f, z)$  is expressed in the exponential form of a Taylor series to derive a closed-form expression for spectral shift in frequency domain as [9], [16], [30]

$$\begin{aligned}
R(f, z) &= f^n = e^{n \cdot \ln(f)} \\
&= e^{[n \cdot \ln(f_c) + n \cdot \ln(1 + (f - f_c)/f_c)]} \\
&\approx f_c^n \cdot e^{n \cdot [(f - f_c)/f_c - (f - f_c)^2/(2f_c^2)]} \\
&\propto e^{-[n \cdot (f^2 - 4f_c f)/(2f_c^2)]}.
\end{aligned} \tag{4}$$

Eq. (4) ignores the higher order terms of the Taylor series expansion. Although the parameter  $n$  can vary from 0 for specular scattering to 4 for Rayleigh scattering, it is assumed to be between 1 to 2 for human tissue.

### B. Spectral Normalization-Based Average Attenuation Estimation Using the Weighted Nearest Neighbor Method

In estimating the AC by minimizing the system effect, the same transducer with identical settings is used to acquire RF data from the tissue sample and a reference TMP. The reference TMP has a known AC and approximately equal sound speed to that of the sample tissue. The power spectrum of the sample tissue at a particular depth is normalized by the power spectrum of the reference TMP for the same depth to minimize the system effects. Exploiting this system-effect minimization process, we propose a spectral normalization-based method where an average linear-regression line is fitted over the normalized half-power bandwidth of the power spectrum, and some spectral parameters such as average midband fit, average spectral slope, and average intercept are estimated. The average regression line is computed from the weighted average of regression lines fitted over nearest neighbor (NN) blocks.

For the reference and sample intensity spectra  $F_r(f, z)$  and  $F_s(f, z)$ , respectively, (1) can be rewritten as

$$F_r(f, z) = T(f) \cdot D_r(f, z) \cdot A_r(f, z) \cdot R_r(f, z), \tag{5}$$

$$F_s(f, z) = T(f) \cdot D_s(f, z) \cdot A_s(f, z) \cdot R_s(f, z), \tag{6}$$

where the subscripts r and s denote the reference and sample, respectively. For the same average sound speed in the reference and sample tissues, the diffraction terms can be written as  $D_r(f, z) = D_s(f, z)$ . Dividing (6) by (5), using (3), and expressing  $\beta$  in decibels per centimeter per megahertz [i.e.,  $\beta$  (Np/cm/MHz) = 8.686  $\times$   $\beta$  (dB/cm/MHz)] yields [26]

$$\begin{aligned}
F(f, z) &= \frac{F_s(f, z)}{F_r(f, z)} = \frac{A_s(f, z) \cdot R_s(f, z)}{A_r(f, z) \cdot R_r(f, z)} \\
&= \frac{R_s(f, z) \cdot 10^{-2\beta_s f z/10}}{R_r(f, z) \cdot 10^{-2\beta_r f z/10}} \\
&= \frac{R_s(f, z)}{R_r(f, z)} \cdot 10^{2(\beta_r - \beta_s) f z/10}.
\end{aligned} \tag{7}$$

Taking the logarithm on both sides of (7) yields

$$10 \log[F(f, z)] = 10 \log \left[ \frac{R_s(f, z)}{R_r(f, z)} \right] + 2\alpha z, \tag{8}$$

where  $\alpha = (\beta_r - \beta_s)/f$ .

Some quantitative acoustic phenomena are modeled in [31] by using some parameters derived from the normalized spectrum analysis. To define these parameters, a regression line is fitted over a usable bandwidth (i.e., approximately at  $-6$  dB) of the normalized power spectrum of the sample tissue. From this regression line, three spectral parameters, namely, the spectral intercept at zero frequency ( $I$ ), midband fit ( $M$ ), and slope of the line ( $s$ ) can be estimated, and they convey significant frequency-domain information about the tissue element. These parameters were originally used in [31] as quantitative measures for tissue characterization. The lower and upper cutoff frequencies,  $f_l$  and  $f_h$ , respectively, for the log power spectra are defined in such a way that both spectra shall have equal data length within the usable bandwidth. At a particular depth  $z$ , the fitted linear-regression line as a function of frequency over the usable bandwidth of the log power spectrum defined in (8) can be expressed as [32]

$$P_\alpha(f) = P(f) + 2\alpha z, \tag{9}$$

where  $P_\alpha(f)$  is the regression line value at a particular frequency  $f$  in the presence of a linear frequency-dependent attenuation  $\alpha$  (in decibels per centimeter).  $P(f)$  corresponds to  $P_\alpha(f)$  at  $z = 0$ , which can be assumed to be a fitted straight line over  $10 \log[R_s(f, z)/R_r(f, z)]$  in (8) and can be expressed as [see Fig. 1]

$$P(f) = I + sf. \tag{10}$$

We estimate another parameter, midband fit  $M = I + sf_c$ , where  $f_c$  is the center frequency of the usable bandwidth. The estimation of these parameters is graphically shown in Fig. 1. Because the estimated amplitude of the whole log power spectrum is noisy, use of usable bandwidth and the spectral parameters increases the robustness of the method. For a block power spectrum corresponding to a single tissue point ( $i_s, j_s$ ) in the AC map, (9) can be rewritten with these spectral parameters as

$$\begin{aligned}
P_\alpha^{(i_s, j_s)}(f) &= P^{(i_s, j_s)}(f) + 2(\beta_r - \beta_s) f z \\
&= I + sf + 2(\beta_r - \beta_s) f z \\
&= I + [s + 2(\beta_r - \beta_s) z] f.
\end{aligned} \tag{11}$$

Here, parameters  $I$  and  $s$  shall be considered instantaneous for a particular tissue point ( $i_s, j_s$ ) unless otherwise specified. Thus, with the presence of linear frequency-dependent attenuation, the expressions for the spectral intercept  $I_\alpha$ , midband fit  $M_\alpha$ , and slope of the regression line  $s_\alpha$  can be written as

$$I_\alpha = I, \tag{12}$$

$$M_\alpha = I + [s + 2(\beta_r - \beta_s) z] f_c, \tag{13}$$

$$s_\alpha = s + 2(\beta_r - \beta_s) z. \tag{14}$$

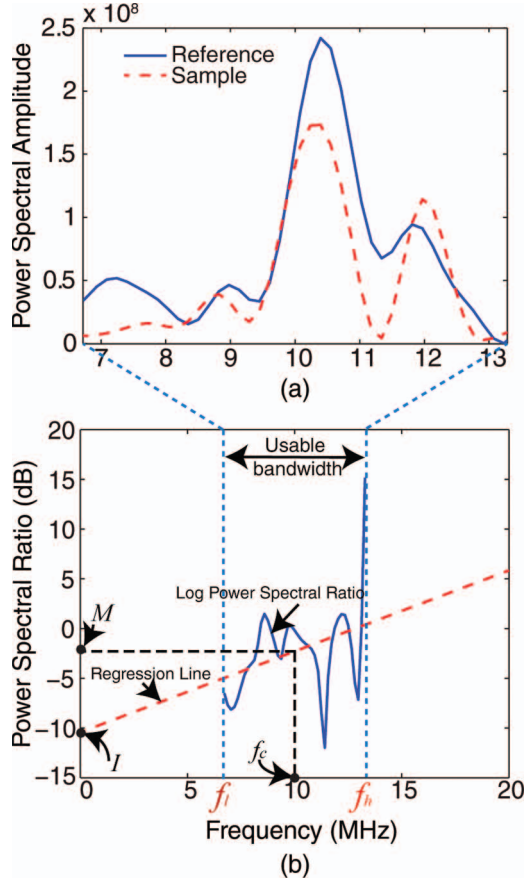


Fig. 1. Illustration of the spectral parameters estimation from the normalized power spectrum (in decibels) of usable bandwidth. (a) The sample and reference spectra over  $-6$ -dB bandwidth, and (b) estimation of the spectral parameters from the fitted and extrapolated regression line over the log power spectral ratio.

Note that the attenuation affects the slope and midband fit, but not the intercept. The invariance of intercept in the presence of tissue attenuation has proved to be fairly accurate in our experience. A similar observation is also reported in [33].

Under the assumption that the tissue attenuation does not change abruptly, the slope of the slope  $s$  versus depth plot, according to (14), will give us the local value of  $(\beta_r - \beta_s)$  in decibels per centimeter per megahertz. However, to utilize all of the computed spectral parameters for robust AC estimation, we can rewrite (13) as

$$I - M_\alpha + sf_c + 2(\beta_r - \beta_s)zf_c = 0. \quad (15)$$

Let  $Y = (I - M_\alpha + sf_c)/2f_c$  and  $X = z$ . Then, (15) can be rewritten as

$$Y + (\beta_r - \beta_s)X = 0. \quad (16)$$

Because the intercept ( $I$ ), slope ( $s$ ), and center frequency ( $f_c$ ) are assumed constant (i.e., independent of attenuation), (16) can be considered as a straight line giving an indirect relation between the drift in the midband fit val-

ues with depth resulting from attenuation. Now, from the slope  $\gamma$  of the regression line that fits (16), we can estimate the local AC (in decibels per centimeter per megahertz) as

$$\beta_s = \beta_r + \gamma. \quad (17)$$

Using average block power spectra in (5) and (6) generated from large spatial signal blocks as in [16], AC can be estimated from (17). But this approach is not suitable for *in vivo* data because tissues of different pathologies may reside within this large signal block area. Therefore, to estimate average AC only from a small neighborhood region, and also to improve the consistency and accuracy, we devise a new technique of average AC estimation by using the weighted nearest neighbors. We assume that the attenuation coefficients of neighboring tissues are almost the same because of their physical proximity. Although human tissue is heterogeneous in nature, it is shown in [25] that the typical heterogeneous tissue can be modeled with several small homogeneous subregions.

Therefore, to improve the accuracy and reliability of the estimate, an average regression line is calculated as the weighted average of regression lines of the nearest neighbor, and is given by

$$\bar{P}_\alpha^{(i_s, j_s)}(f) = \frac{\sum_{i_0=i_s-L_a}^{i_s+L_a} \sum_{j_0=j_s-L_1}^{j_s+L_1} w^{(i_s, j_s)}(i_0, j_0) \times P_\alpha^{(i_0, j_0)}(f)}{\sum_{i_0=i_s-L_a}^{i_s+L_a} \sum_{j_0=j_s-L_1}^{j_s+L_1} w^{(i_s, j_s)}(i_0, j_0)}, \quad (18)$$

where  $\bar{P}_\alpha^{(i_s, j_s)}(f)$  denotes the average value of  $P_\alpha^{(i_s, j_s)}(f)$  and  $w^{(i_s, j_s)}$  is the exponential weight function for an interrogative point  $(i_s, j_s)$  on the 2-D AC map, defined as

$$w^{(i_s, j_s)}(i_0, j_0) = e^{-\lambda_a(i_0-i_s)-|\lambda_l(j_0-j_s)|}, \quad (19)$$

where  $\lambda_a$  and  $\lambda_l$  denote the weighting factors in the axial and lateral directions, respectively, and  $i_s - L_a \leq i_0 \leq i_s + L_a$  and  $j_s - L_1 \leq j_0 \leq j_s + L_1$ .  $L_a$  and  $L_1$  are the NN factors in the axial and lateral directions, respectively. We can see from (19) that  $w^{(i_s, j_s)}(i_0, j_0)$  is maximal (i.e., unity) at  $(i_0, j_0) = (i_s, j_s)$ . The weight function  $w^{(i_s, j_s)}$  is defined in such a way that the block power spectral regression lines of increasing distance are properly weighted to be progressively less emphasized (see Fig. 2). We use  $\lambda_a = \lambda_l = 0.50$  for the SNAAE method in this study, unless otherwise specified.

The effect of using the weighted average of NN regression lines is shown in Fig. 3. In this figure, we see that the instantaneous regression lines have variations in their spectral intercept values as well as in the midband fit values, although they are selected from the proximal homogeneous tissue points. This fluctuation in spectral parameters may be attributed to the noise in the power spectra over the  $-6$ -dB bandwidth. To minimize this noise effect, an average regression line can be estimated using the proposed weighted nearest neighbors and henceforth average



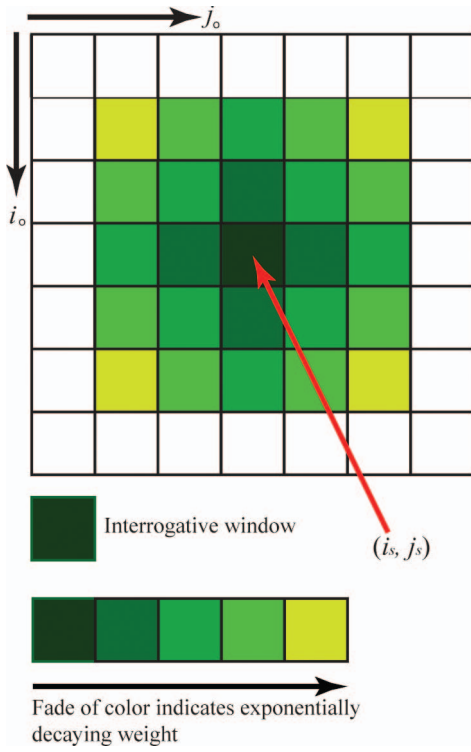



Fig. 2. Illustration of the neighboring blocks' contribution in the estimation of effective attenuation coefficient (AC) for an investigating point  $(i_s, j_s)$ . Note that some neighboring block regression lines are weighted exponentially to estimate the average regression line for the block at  $(i_s, j_s)$  point. 

spectral parameters (i.e., average midband fit, average slope, and average spectral intercept) can be estimated from this average regression line.

Because  $P_\alpha^{(i_s, j_s)}(f) = I + sf + 2(\beta_r - \beta_s)zf$  [see (11)], (18) yields,

$$I_{\text{avg}} = \frac{\sum_{i_0=i_s-L_a}^{i_s+L_a} \sum_{j_0=j_s-L_1}^{j_s+L_1} w^{(i_s, j_s)}(i_0, j_0) \times I}{\sum_{i_0=i_s-L_a}^{i_s+L_a} \sum_{j_0=j_s-L_1}^{j_s+L_1} w^{(i_s, j_s)}(i_0, j_0)}, \quad (20)$$

$$s_{\text{avg}} = \frac{\sum_{i_0=i_s-L_a}^{i_s+L_a} \sum_{j_0=j_s-L_1}^{j_s+L_1} w^{(i_s, j_s)}(i_0, j_0) \times s}{\sum_{i_0=i_s-L_a}^{i_s+L_a} \sum_{j_0=j_s-L_1}^{j_s+L_1} w^{(i_s, j_s)}(i_0, j_0)}. \quad (21)$$

Then, by using  $\bar{P}_\alpha^{(i_s, j_s)}(f)$ ,  $I_{\text{avg}}$ , and  $s_{\text{avg}}$ , we can rewrite (10) and (11) as

$$\bar{P}^{(i_s, j_s)}(f) = I_{\text{avg}} + s_{\text{avg}}f, \quad (22)$$

$$\begin{aligned} \bar{P}_\alpha^{(i_s, j_s)}(f) &= I_{\text{avg}} + s_{\text{avg}}f + 2(\beta_r - \beta_s)zf \\ &= I_{\text{avg}} + [s_{\text{avg}} + 2(\beta_r - \beta_s)z]f. \end{aligned} \quad (23)$$

Now, for average midband fit, we can write

$$M_{\text{avg}} = I_{\text{avg}} + [s_{\text{avg}} + 2(\beta_r - \beta_s)z]f_c. \quad (24)$$

For average AC estimation, let  $Y_{\text{avg}} = (I_{\text{avg}} - M_{\text{avg}} + s_{\text{avg}}f_c)/2f_c$  and  $X = z$ , and then (24) can be rewritten as

$$Y_{\text{avg}} + (\beta_r - \beta_s)X = 0. \quad (25)$$

Now, from the slope  $\gamma_{\text{avg}}$  of the regression line that fits (25), we can estimate the local AC (in decibels per centimeter per megahertz) as

$$\beta_s = \beta_r + \gamma_{\text{avg}}. \quad (26)$$

In Fig. 4, we show plots of the estimated  $Y$ ,  $Y_{\text{avg}}$ , and the theoretical line derived from (25) versus depth within an arbitrary scan-line segment of length 1.5 cm of a CIRS (Computerized Imaging Reference Systems Inc., Norfolk, VA) ultrasound phantom data set A (see Section III for

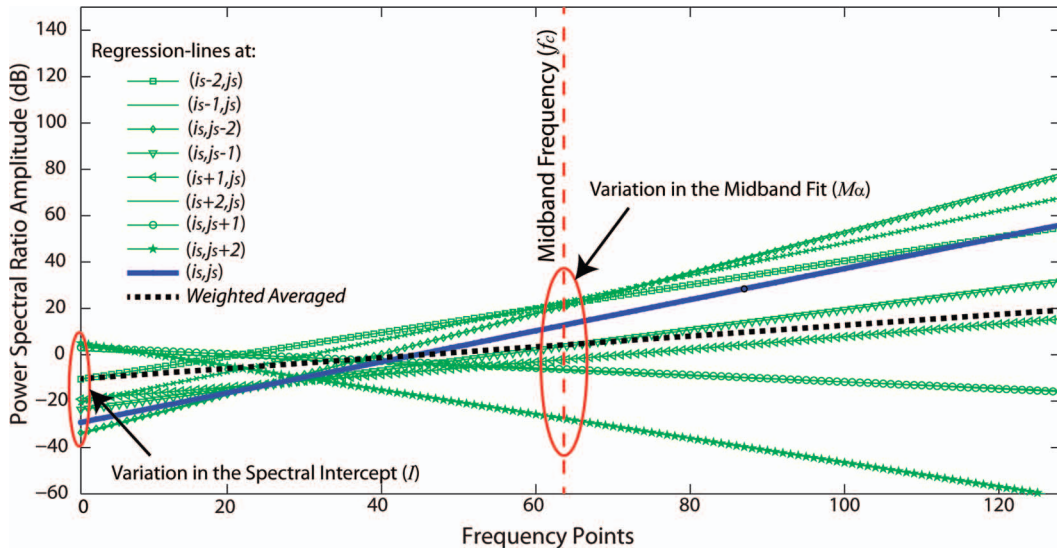



Fig. 3. Representation of instantaneous regression lines  $P_\alpha^{(g_s, h_s)}(f)$ ;  $(i_s - 2 \leq g_s \leq i_s + 2$  and  $j_s - 2 \leq h_s \leq j_s + 2)$  and the proposed weighted averaged regression line  $[\bar{P}_\alpha^{(i_s, j_s)}(f)]$  for attenuation coefficient (AC) estimation at  $(i_s, j_s)$  using the experimental phantom against the Fourier frequency points. 

details) for three different SNRs (40, 30, and 20 dB) along with that for the original RF data. We have added zero-mean white Gaussian noise of different levels to the measured RF data to observe its effect on the proposed estimates. For consistency analysis, 100 realizations of the noisy RF data sets are used to generate Figs. 4(b)–4(d). From Fig. 4(a), we see for the original RF data that the instantaneous values obtained from the SNAAE method for  $L_a = L_l = 0$  vary greatly with respect to the theoretical line, whereas the estimated  $Y_{\text{avg}}$  by the proposed SNAAE method for  $L_a = L_l = 5$  closely fits the theoretical line. As is evident from Figs. 4(b)–4(d), the estimated  $Y_{\text{avg}}$  is much more accurate and consistent than  $Y$  at all SNRs. The lack of fit results in a bias of 0.0606, 0.0634, and 0.0778 dB/cm/MHz in the final estimates at 40, 30, and 20 dB SNR, respectively, with respect to the true AC value. The increase in bias resulting from additive noise in the final estimate of AC for the data set A (with data set B as reference) is also observed to be very low up to 25 dB SNR (0.0102 dB/cm/MHz at 25 dB SNR) for the SNAAE method with  $L_a = L_l = 5$ . It is, therefore, evident that the SNAAE method with nearest neighbors (i.e.,  $L_a = L_l \neq 0$ ) is more accurate for noise-robust acoustic attenuation estimation than the instantaneous method.

### C. Spectral Shift-Based Average Attenuation Estimation Using the Weighted Nearest Neighbor Method

The spectral shift-based attenuation estimation methods usually estimate the AC from the slope of the center frequency downshift with respect to depth; however, these methods give estimates with high variance [34] and typically use large spatial signal blocks to generate stable block power spectra to estimate tissue AC. As in the preceding section, the AC of a tissue is assumed to be fairly identical to the AC of its neighboring tissues because of their close physical proximity. To avoid using large spatial signal blocks, we propose a novel technique for average attenuation estimation by measuring the average spectral shift with a robust cost function constructed from the exponentially weighted NSCC functions of the nearest neighbor 1-D signal blocks.

The NSCC between two power spectra  $F(f, z_1)$  and  $F(f, z_2)$  that corresponds to an interrogative point  $(i_s, j_s)$  on the 2-D AC map can be calculated as [35]

$$S^{(i_s, j_s)}(f_0) = \frac{\int_{-\infty}^{\infty} F(f + f_0, z_1)F(f, z_2)}{\sqrt{\int_{-\infty}^{\infty} F(f, z_1)^2 \cdot \int_{-\infty}^{\infty} F(f, z_2)^2}}, \quad (27)$$

where  $z_1$  and  $z_2$  ( $> z_1$ ) are two different depths estimated with respect to the transducer face. With the assumption of no abrupt change in the local AC values, the spectral shift  $f_c$  between the power spectra at depths  $z_1$  and  $z_2$  can be derived by substituting for  $T(f)$ ,  $A(f, z)$ , and  $R(f, z)$  from (2), (3), and (4), respectively, in (27) as

$$S^{(i_s, j_s)}(f_0) = \frac{1}{\text{NC}} \int_{-\infty}^{\infty} e^{-(f+f_0-f_c)^2/(2\sigma^2)} \cdot e^{-4\beta(f+f_0)z_1} \cdot e^{-n \cdot ((f+f_0)^2 - 4f_c(f+f_0))/(2f_c^2)} \cdot e^{-(f-f_c)^2/2\sigma^2} \cdot e^{-4\beta f z_2} \cdot e^{-n \cdot (f^2 - 4f_c f)/(2f_c^2)} df, \quad (28)$$

where NC is a normalization constant defined as

$$\text{NC} = \sqrt{\int_{-\infty}^{\infty} F(f, z_1)^2 \cdot \int_{-\infty}^{\infty} F(f, z_2)^2}. \quad (29)$$

Simplifying (28), we obtain

$$S^{(i_s, j_s)}(f_0) = \frac{1}{\text{NC}} \int_{-\infty}^{\infty} e^{-[A/(2\sigma^2 f_c^2)]} df, \quad (30)$$

where

$$A = 2B \left( f + \frac{C}{2B} \right)^2 + \frac{2BD - C^2}{2B}, \quad (31)$$

and

$$B = f_c^2 + n\sigma^2, \quad (32)$$

$$C = Bf_0 + 2f_c^3 + 4\sigma^2\beta(z_1 + z_2)f_c^2 - 4n\sigma^2 f_c, \quad (33)$$

$$D = Bf_0^2 + 2(4\sigma^2\beta z_1 f_c^2 + f_c^3 - 2n\sigma^2 f_c)f_0 + 2f_c^4. \quad (34)$$

Further simplifying, the NSCC function can be written as

$$S^{(i_s, j_s)}(f_0) = \frac{1}{\text{NC}} \cdot e^{[(C^2 - 2BD)/(4\sigma^2 f_c^2 B)]} \cdot \int_{-\infty}^{\infty} e^{-[(f+C/(2B))^2/((\sigma^2 f_c^2)/B)]} df. \quad (35)$$

From the standard integral form  $\int_{-\infty}^{\infty} e^{-ax^2} dx = \sqrt{\pi/a}$ , we can rewrite (35) as

$$S^{(i_s, j_s)}(f_0) = \frac{1}{\text{NC}} \cdot e^{[E/(4\sigma^2 f_c^2)]} \cdot \sqrt{\frac{\sigma^2 f_c^2 \cdot \pi}{B}}, \quad (36)$$

where

$$E = \frac{C^2 - 2BD}{B}. \quad (37)$$

To find the spectral shift from the maximum of the NSCC function, we differentiate  $S^{(i_s, j_s)}(f_0)$  with respect to  $f_0$ , and equate it to zero as

$$\frac{dS^{(i_s, j_s)}(f_0)}{df_0} = \frac{1}{\text{NC}} \cdot \sqrt{\frac{\sigma^2 f_c^2 \cdot \pi}{B}} \cdot e^{[E/(4\sigma^2 f_c^2)]} \cdot \frac{dE}{df_0} = 0. \quad (38)$$

After simplifying, we obtain

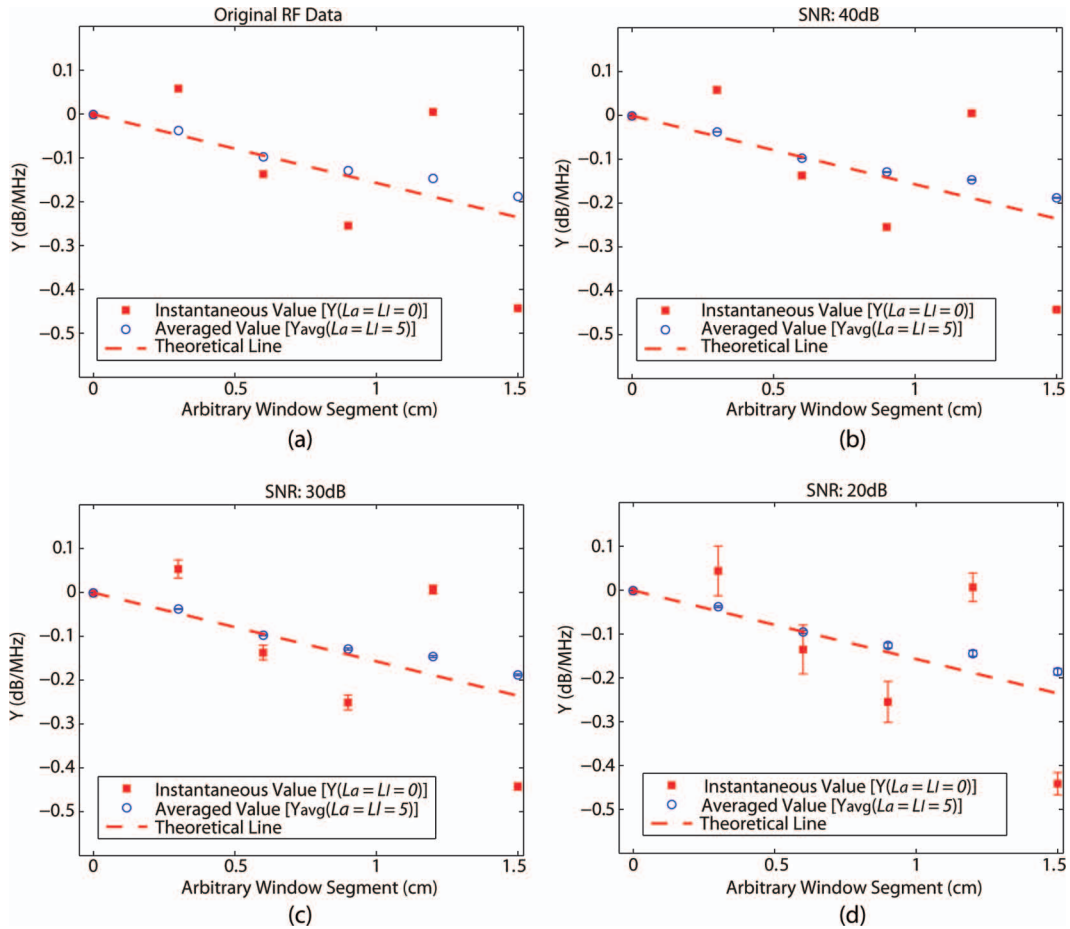


Fig. 4. Illustration of the estimated  $Y$ ,  $Y_{\text{avg}}$ , and the theoretical line within an arbitrary 1.5 cm window segment for (a) no additive noise, (b) 40 dB SNR, (c) 30 dB SNR, and (d) 20 dB SNR tissue-mimicking phantom (TMP) data. The theoretical line is derived from (24). In (b), (c), and (d), 100 realizations of the noisy RF data sets are used. The true attenuation coefficient (AC) values for the reference and sample TMP are 0.7 and 0.5 dB/cm/MHz, respectively.

$$\frac{f_0}{(z_1 - z_2)} = \frac{df_c(z)}{dz} = -\frac{4\sigma^2\beta}{1 + \frac{n\sigma^2}{f_c^2}}, \quad (39)$$

where  $f_c(z)$  is the center frequency at depth  $z$ . Because the value of the parameter  $n$  is assumed to be between 1 and 2 for human tissue, and the ultrasound center frequency  $f_c$  is generally greater than the standard deviation  $\sigma$  of the transmitted pulse, (39) can be simplified as

$$\beta(\text{Np/cm/MHz}) = -\frac{1}{4\sigma^2} \cdot \frac{df_c(z)}{dz}. \quad (40)$$

Note that although we calculate the normalized spectral cross-correlation in (27) to further use the correlation function in the cost function, (40) is structurally the same as that derived in [16] for AC estimation. However, in [16], (40) gives a single estimate of AC for a very large interrogative signal block. However, this approach is often not suitable for *in vivo* data because tissues of different pathologies may reside within this large signal block area. Therefore, to estimate an average AC only from a small

neighborhood region, we use interrogative and weighted nearest neighbor NSCC values to form a cost function. That is why NSCC estimation is essential for using it in (41). Otherwise, a higher valued false cross-correlation peak with less weight may bias the desired estimate.

We now define a cost function from the weighted nearest neighbor NSCC functions in both the axial and lateral directions to estimate an average spectral shift and, thus, an average attenuation coefficient. Because the ACs of proximal tissues are more similar relative to the distant ones, an exponential weighting is performed to ensure relatively larger weights for the nearest NSCC functions. The cost function is defined as

$$J^{(i_s, j_s)}(f_0) = \sum_{i_0=i_s-L_a}^{i_s+L_a} \sum_{j_0=j_s-L_l}^{j_s+L_l} w^{(i_s, j_s)}(i_0, j_0) S^{(i_s, j_s)}(f_0), \quad (41)$$

where  $w^{(i_s, j_s)}$  is the exponential weight function for an interrogative point  $(i_s, j_s)$  on the 2-D AC map and is defined as

$$w^{(i_s, j_s)}(i_0, j_0) = e^{-|\lambda_a(i_0 - i_s)| - |\lambda_l(j_0 - j_s)|}. \quad (42)$$

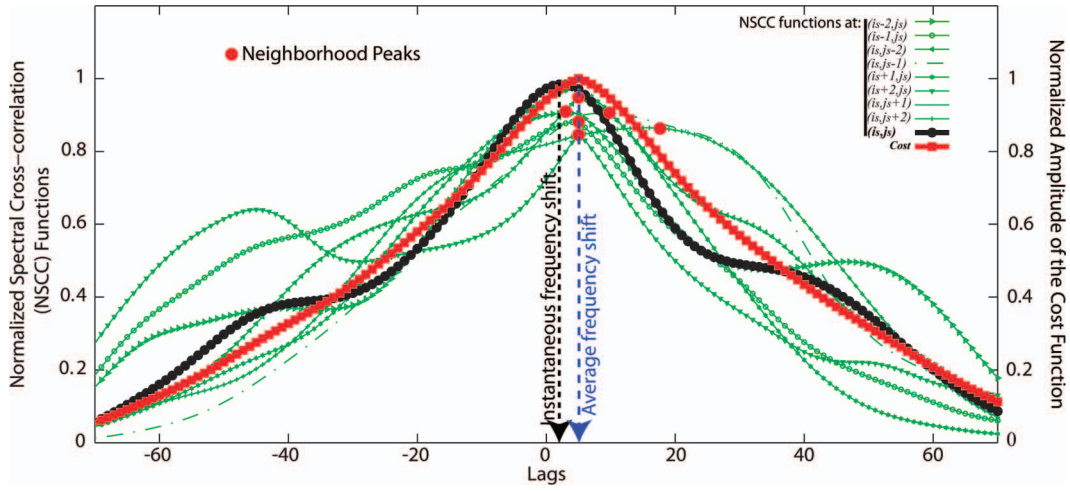


Fig. 5. Representation of instantaneous normalized spectral cross-correlation (NSCC) functions  $S^{(g_s, h_s)}(f_0)$ ; ( $i_s - 2 \leq g_s \leq i_s + 2$  and  $j_s - 2 \leq h_s \leq j_s + 2$ ), and the proposed cost function  $[J^{(i_s, j_s)}(f_0)]$  for attenuation coefficient (AC) estimation at  $(i_s, j_s)$  using the experimental phantom against the spectral shift (i.e., lags).

Here,  $\lambda_a$  and  $\lambda_l$  denote the weighting factors in the axial and lateral directions, respectively, and  $i_s - L_a \leq i_0 \leq i_s + L_a$  and  $j_s - L_l \leq j_0 \leq j_s + L_l$ .  $L_a$  and  $L_l$  are the NN factors in the axial and lateral directions, respectively. We can see from (41) that  $w^{(i_s, j_s)}(i_0, j_0)$  is maximal (i.e., unity) at  $(i_0, j_0) = (i_s, j_s)$ . The weight function  $w^{(i_s, j_s)}$  is defined such that the NSCC functions of increasing distance are properly weighted to be progressively less emphasized (see Fig. 2). We do not incorporate any instantaneous NSCC functions from the neighborhood into the cost function if the corresponding instantaneous spectral downshift is outside the practical range. We use  $\lambda_a = \lambda_l = 0.1$  for the SCAAE method in this study unless otherwise specified.

The effect of using such a cost function is shown in Fig. 5. In this figure, we see that the NSCC functions estimated from the instantaneous signal blocks have variations in their peak positions, although they are selected from the proximal homogeneous tissue points. Some of the NSCC functions do not even have distinct peaks, whereas the proposed cost function depicts a clear peak. Therefore, the proposed cost function can be used to calculate reliable average spectral shifts along the depth.

The peaks of  $J^{(i_s, j_s)}(f_0)$  can be calculated by using any subsample interpolation algorithm (e.g., cosine interpolation, parabolic interpolation) for different frequency shifts ( $f_c$ ). However, in this work, the average spectral shift at  $(i_s, j_s)$  is estimated using the cosine interpolation as

$$f_{\text{avg}} = \arg \max_{f_0} \{J^{(i_s, j_s)}(f_0)\}. \quad (43)$$

Using the estimated  $f_{\text{avg}}$ , (38) can be modified as

$$\frac{f_{\text{avg}}}{(z_1 - z_2)} = \frac{df_{c, \text{avg}}(z)}{dz} = -\frac{4\sigma^2\beta}{1 + \frac{n\sigma^2}{f_{c, \text{avg}}^2}}. \quad (44)$$

Because of the use of focused array transducers in clinical settings, the properties of the power spectra are distorted in the pre- and post-focal regions. This effect becomes evident in the slope of the straight line that fits the center frequency downshift along depth. Thus, the AC is under- and over-estimated in the pre- and post-focal regions, respectively [27]. To correct for this diffraction effect, a reference phantom of known attenuation properties can be used [16]. Backscattered RF signals are obtained for both the sample tissue and the reference phantom with the same transducer (i.e., center frequency, sampling frequency, focus, depth, etc.) and power settings. Because the AC of the reference phantom is known, we can plot its theoretical center frequency downshift with respect to depth, with  $f_c$  as the starting frequency near the transducer face (see Fig. 7). Again, we can estimate the AC of the reference phantom by the proposed method. From these theoretical and measured center frequency downshift plots, we can estimate the contribution of the diffraction effect by subtracting the estimated value from the theoretical one along depth. This contribution is normalized with respect to the frequency at each depth and is subsequently used for the diffraction correction of the sample tissue. A linear-fit window of length 20 mm over the diffraction-corrected local spectral shift is applied and finally, an average AC can be estimated from the modified (40) as

$$\beta(\text{Np/cm/MHz}) = -\frac{1}{4\sigma^2} \cdot \frac{df_{c, \text{avg}}(z)}{dz}. \quad (45)$$

In (45),  $\sigma$  is to be estimated from the mean full-width at half-maximum (FWHM) of the stable echo spectra. It is shown in [16] and [24] that stable spectra are achieved by using a large spatial signal block. However, because we use a 1-D signal block which contains three 50% axially overlapped signal windows, we estimate an exponentially



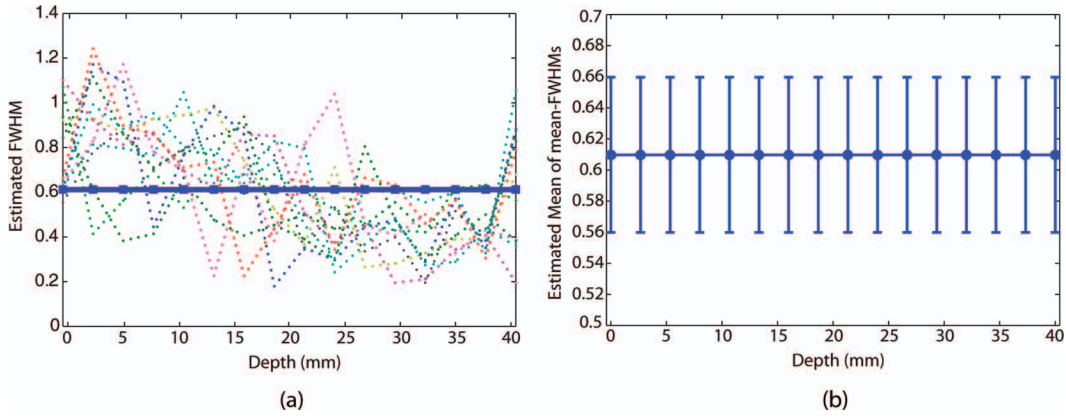


Fig. 6. Estimated full-width at half-maximum (FWHM) of the backscattered echo power spectra. (a) Instantaneous FWHMs ( $\eta$ ) of the interrogative and neighboring scan-lines ( $L_1 = 5$ ) are shown with dotted lines. Exponentially weighted average FWHM ( $\eta_w$ ) estimated from the means ( $\bar{\eta}$ ) of each instantaneous FWHM ( $\eta$ ) is plotted as a constant solid line. (b) Mean of  $\eta_w$  estimated from all the scan-lines in a RF frame. In all the cases, the center frequency of the transmit pulse is 10 MHz with true FWHM 0.65 and the attenuation coefficient (AC) is 0.5 dB/cm/MHz.

weighted average FWHM  $\eta_w$  for the interrogative scan-line as

$$\eta_w(j_s) = \frac{\sum_{j_0=j_s-L_1}^{j_s+L_1} m(j_0)\bar{\eta}(j_0)}{\sum_{j_0=j_s-L_1}^{j_s+L_1} m(j_0)}, \quad (46)$$

where

$$m(j_0) = e^{-|\kappa_1(j_0-j_s)|}, \quad (47)$$

where  $\kappa_1$  denotes the weighting factor in the lateral direction,  $j_s - L_1 \leq j_0 \leq j_s + L_1$ , and  $L_1$  is the NN factor in the lateral direction, and  $\bar{\eta}(j_0)$  is the mean of instantaneous FWHM  $\eta(j_0)$  along depth for the interrogative scan-line at  $j_0$ . We can see from (47) that  $m(j_0)$  is maximum (i.e., unity) at  $j_0 = j_s$ . The weight function  $m$  is defined in a way such that the mean-FWHMs  $\bar{\eta}(j_0)$  of increasing distance are properly weighted to be progressively less emphasized. We use  $\kappa_1 = 0.1$ .

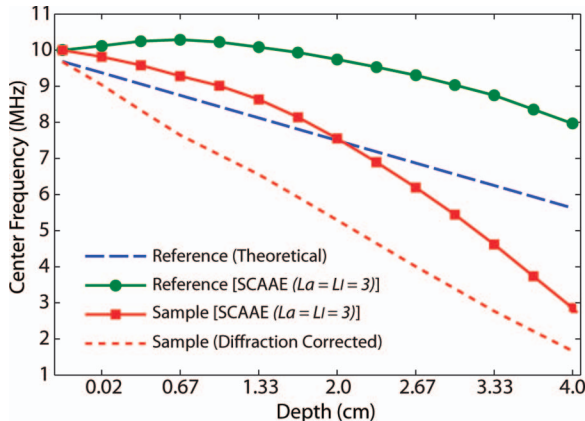


Fig. 7. Diffraction compensation with respect to the reference spectra. The attenuation coefficient (AC) of the reference and sample are 0.5 and 0.7 dB/cm/MHz, respectively. The beam focus is at 2 cm from the transducer face.

We show the instantaneous FWHM  $\eta$  along the depth for interrogative and neighboring scan-lines with dotted lines in Fig. 6(a). We also plot the exponentially weighted average FWHM  $\eta_w$  for the interrogative scan-line with a solid line in Fig. 6(a). The true FWHM is 0.65 for the transducer we use. In Fig. 6(b), we show the mean of  $\eta_w$  estimated from all the scan-lines in the RF frame. We can see from Fig. 6(b) that the mean of  $\eta_w$  is close to the true FWHM value (i.e., 0.65) with very low standard deviation. Therefore, we can use the estimated weighted average FWHM  $\eta_w$  for calculating  $\sigma$ .

In Fig. 8, we show plots of the center frequency ( $f_c$ ) downshift estimated by the SCAAEE ( $L_a = L_1 = 5$ ) and spectral shift [16] methods, and the theoretical spectral downshift derived from (44) versus depth within an arbitrary scan-line segment of length 1.5 cm of the CIRS ultrasound phantom data set A (see Section III for details) for three different SNRs (40, 30, and 20 dB) along with that for the original RF data. As before, noise effect on the proposed estimates is observed by adding zero-mean white Gaussian noise of different levels to the measured RF data. For consistency analysis, 100 realizations of the noisy RF data sets are used to generate Figs. 8(b)–8(d). Here again, we see that the center frequency downshift values obtained from the spectral shift method varies much with respect to the theoretical spectral downshift. In addition, with the decrease in SNR, the standard deviation of the center frequency downshift obtained from the spectral shift method increases significantly [see Figs. 8(b)–8(d)]. In contrast, the estimated average center frequency ( $f_{c,avg}$ ) downshift by the proposed SCAAEE method with nearest neighbors (i.e.,  $L_a = L_1 \neq 0$ ) closely fits the theoretical center frequency downshift for up to 30 dB SNR and the estimated standard deviations at different SNRs are also very low [see Figs. 8(b)–8(d)]. The lack of fit results in a bias of 0.0121, 0.0129, and 0.0638 dB/cm/MHz in the final estimates at 40, 30, and 20 dB SNR, respectively, with respect to the true AC value. The increase in bias due to additive noise in the final estimate of AC for the data set

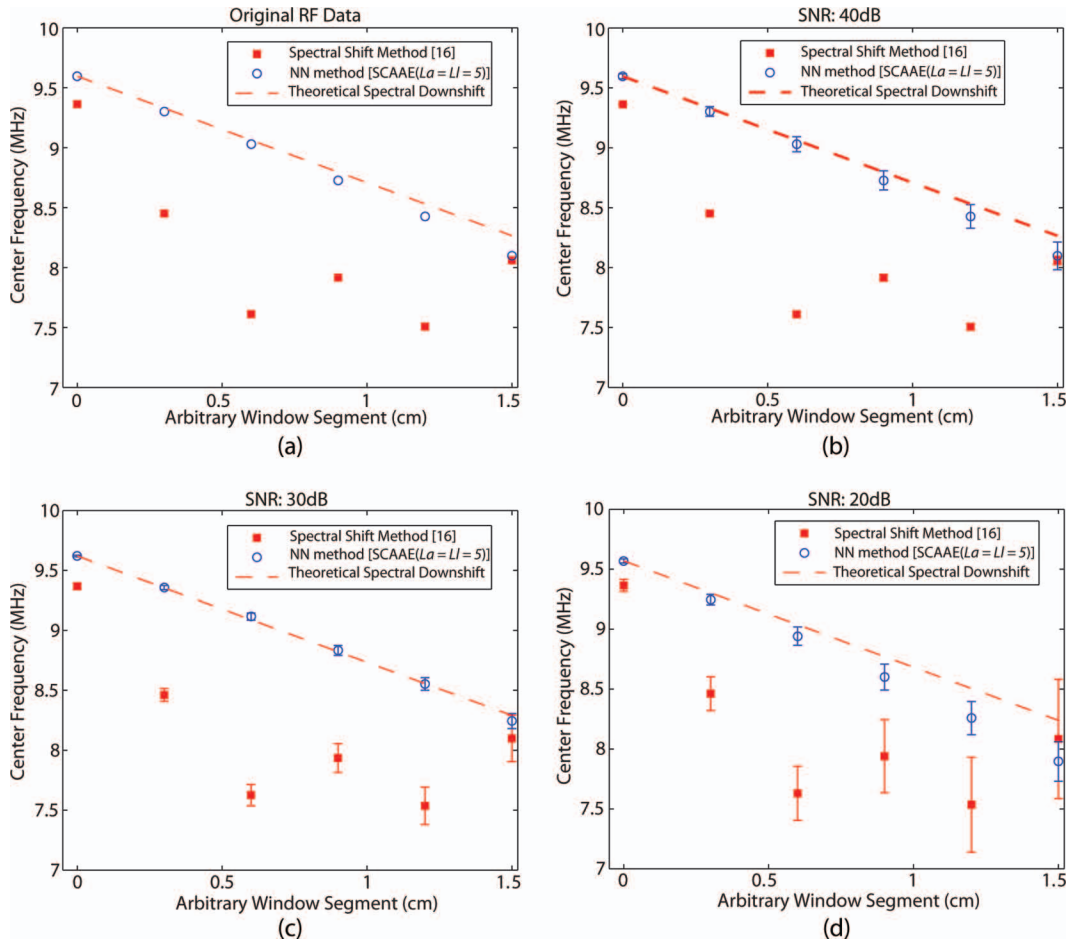


Fig. 8. Illustration of the center frequency downshift within an arbitrary 1.5 cm window segment for (a) no additive noise, (b) 40 dB SNR, (c) 30 dB SNR, and (d) 20 dB SNR tissue-mimicking phantom (TMP) data obtained by the spectral cross-correlation-based average attenuation estimation (SCAAE) ( $L_a = L_l = 5$ ) and spectral shift [16] methods. The theoretical center frequency downshift derived from (44) is also plotted. In (b), (c), and (d), 100 realizations of the noisy RF data sets are used. The true attenuation coefficient (AC) values for the reference and sample TMP are 0.7 and 0.5 dB/cm/MHz, respectively.

A (with TMP data set B as reference) is also observed to be insignificant up to 25 dB SNR (0.0085 dB/cm/MHz at 25 dB SNR) for the SCAAEE method with  $L_a = L_l = 5$ . Fig. 8, therefore, reveals that the center frequency downshift and hence the acoustic attenuation can be better estimated by the proposed SCAAEE than the spectral shift method.

### III. EXPERIMENTAL RESULTS

We test the efficacy as well as provide comparative results of our proposed methods with the spectral shift [16], spectral difference [19], and hybrid [24] methods using the CIRS experimental phantom and the *in vivo* data of a normal female breast.

#### A. Experimental Phantom Results

We have used four sets of TMP data, A, B, C, and D of dimension  $4 \times 4$  cm (except for C, which is  $5 \times 4$  cm),

having homogeneous backgrounds with AC 0.5, 0.7, 0.5, and 0.5 dB/cm/MHz, respectively, to evaluate the performances of the proposed and other three techniques in this paper. The data set C includes a spherical inclusion of radius 0.35 cm, centered at 4 cm below the top surface, having AC 0.95 dB/cm/MHz. The data set D includes a cylindrical inclusion of radius 0.835 cm, centered at 2 cm below the top surface, having AC 0.7 dB/cm/MHz. Because the data sets A and B are homogeneous and do not have any inclusion, we use data sets B, A, B, and B as references for the data sets A, B, C, and D, respectively. The homogeneous background and the inclusions of the TMP are made of Zerdine with sound speed 1540 m/s. These data were acquired at the Bangladesh University of Engineering and Technology (BUET) Medical Center, Dhaka, Bangladesh, by using a SonixTOUCH Research (Ultrasound Medical Corp., Richmond, BC, Canada) scanner integrated with a L14-5/38 probe operating at 10 MHz with 65% bandwidth and at a sampling rate of 40 MHz. During data acquisition, no TGC was used. The focus was set to 2 cm away from the transducer face.

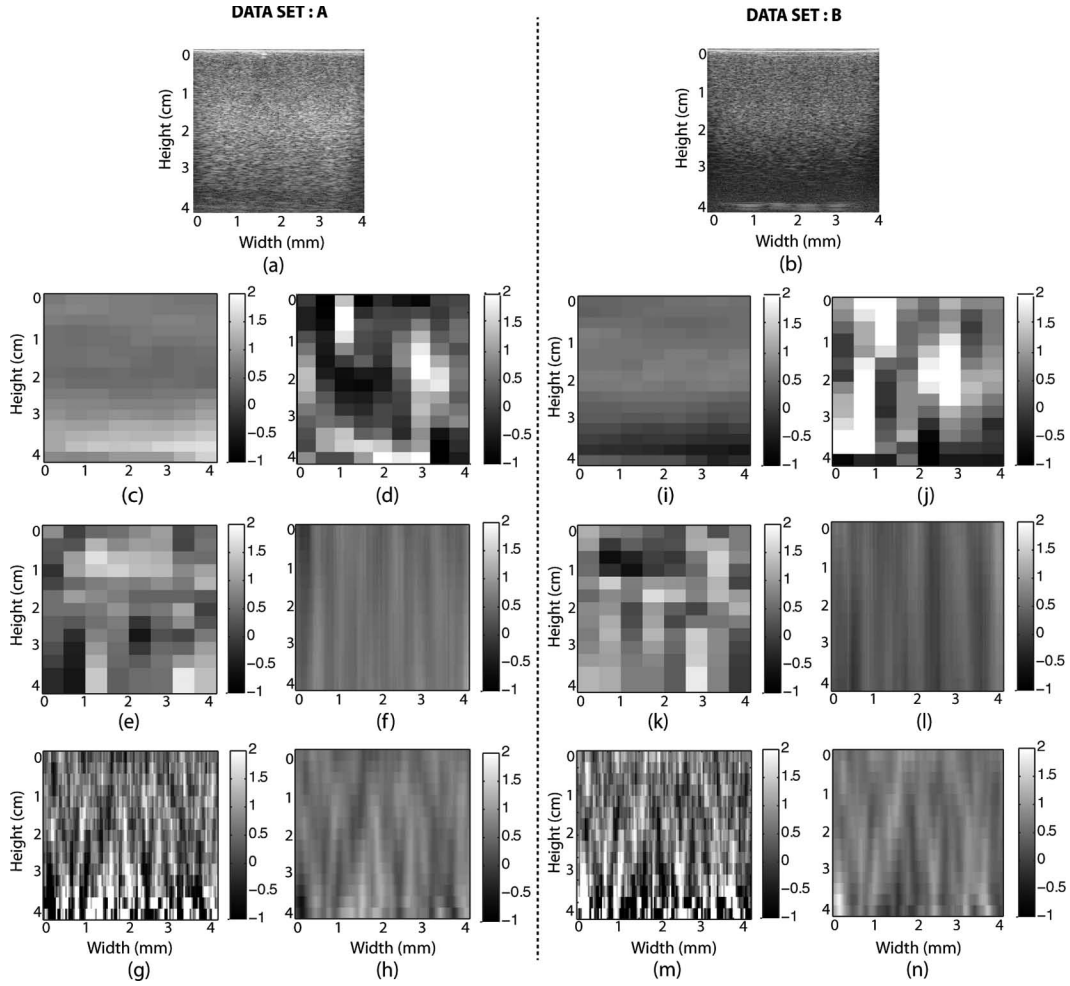


Fig. 9. Illustration of the B-mode and attenuation coefficient (AC) images for tissue-mimicking phantom (TMP) data sets A and B having AC 0.5 and 0.7 dB/cm/MHz, respectively. Figures (a) and (b) represent the B-mode images, AC images (c) and (i) are produced by the spectral difference, (d) and (j) are produced by the hybrid, (e) and (k) are produced by the spectral shift, (f) and (l) are produced by the proposed spectral cross-correlation-based average attenuation estimation (SCAAE) (for  $L_a = L_l = 5$ ), (g) and (m) are produced by the proposed spectral normalization-based average attenuation estimation (SNAEE) (for  $L_a = L_l = 0$ ), and (h) and (n) are produced by the proposed SNAEE (for  $L_a = L_l = 5$ ) methods for the data sets A and B, respectively. Data sets B and A are used as references for the data sets A and B, respectively. The linear fit window length is set to 20 mm.

1) *RF Data Processing*: For the spectral shift, spectral difference and hybrid methods, 50% axially and laterally overlapping 2-D spatial signal blocks are considered for producing stable block power spectrum. In contrast, only 50% axially overlapping 1-D spatial signal blocks are considered for the SNAEE and SCAAEE methods. The axial length of the block should be chosen in such a way that it satisfies the stationarity assumption. In the techniques compared with the proposed methods, the block size is optimized by using the FWHM criterion [16] to obtain stable block power spectra. The block power spectrum is calculated by averaging the STFT estimates of the gated window segments into the block [36]. A 50% axial overlap is used between two successive window segments within a block. Each block contains 25 lateral scan-lines and the power spectrum is estimated from an average of 75 Fourier spectra (in the case of homogeneous background). The dimension of each block is taken to be approximately  $4.70 \times 7.80$  mm in the spectral shift, spectral difference, and

hybrid methods. For all of the methods, the axial length of each 1-D gated window is approximately 2.35 mm and is gated by the Hanning window to minimize the leakage artifacts. The linear fit window is set to 20 mm for estimating the local AC. Considering a fit window of similar length is a general practice in the literature. Therefore, in our proposed methods, we take advantage of using the nearest neighbors from an area that has axial length of approximately 20 mm by setting  $L_a = 5$ . However, the lateral width of the neighborhood region becomes only 3.13 mm if we set  $L_l = 5$  for our proposed methods, in contrast to the traditional large spatial block that takes approximately 7.80 mm (i.e., equivalent to 25 adjacent scan-lines as used in this paper) in the lateral direction. However, in the proposed methods, the effective size of the neighborhood window (in the axial and lateral directions) is smaller than those mentioned previously because of the use of weighting factors  $\lambda_a$  and  $\lambda_l$  [see (19) and (42)].

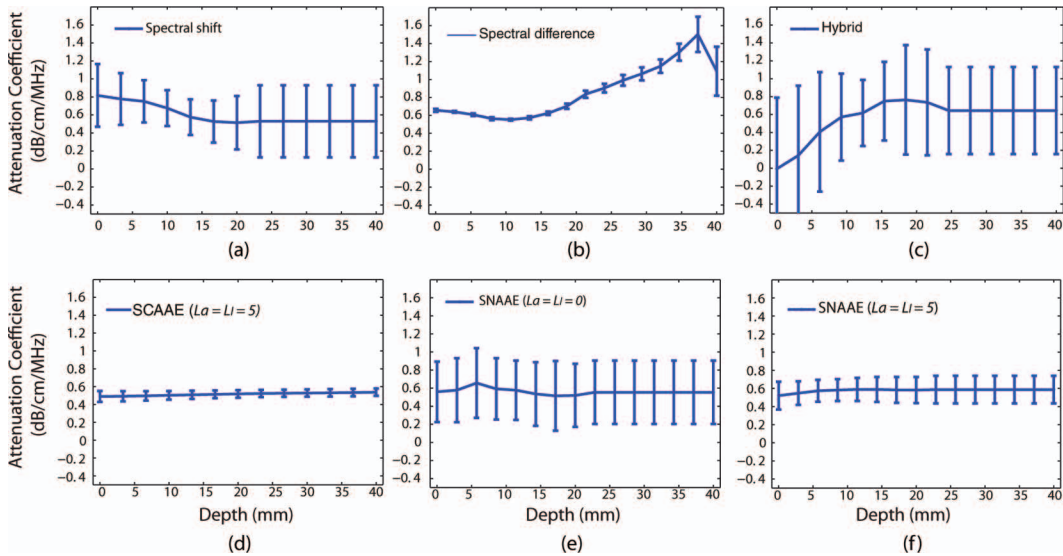


Fig. 10. Illustration of mean attenuation coefficient (AC) profiles generated by different methods for the tissue-mimicking phantom (TMP) data set A having AC 0.5 dB/cm/MHz. Mean profiles are estimated along width for AC maps shown in Figs. 9(c)–9(h) by different methods. Profiles are produced by the (a) spectral shift, (b) spectral difference, (c) hybrid, (d) spectral cross-correlation-based average attenuation estimation (SCAAE) (for  $L_a = L_l = 5$ ), (e) spectral normalization-based average attenuation estimation (SNAAE) (for  $L_a = L_l = 0$ ), and (f) SNAAE (for  $L_a = L_l = 5$ ) methods.

2) *Performance Evaluation Using CIRS TMP*: The AC imaging performance of the proposed and other published techniques for the data sets A and B is shown in Fig. 9. The data sets B and A are used as references for the sample data sets A and B, respectively. Figs. 9(a) and 9(b) represent the homogeneous B-mode images for the sample data sets A and B, respectively. We can see from Fig. 9 that, because of using large spatial signal blocks, a single AC value corresponds to a large spatial region in the AC maps generated by the spectral difference, hybrid,

and spectral shift methods [see Figs. 9(c)–9(e) and Figs. 9(i)–9(k), respectively]. Moreover, the tissue pathology inside a large spatial block must be considered uniform, which is often not realistic for the heterogeneous tissue. However, we can see from Figs. 9(f) and 9(l), generated by the SCAAE method, and Figs. 9(h) and 9(n), generated by the SNAAE method, with  $L_a = L_l = 5$  that the AC values can be generated for all the scan-lines as a result of using the NN concept, and the AC maps are smoother than those produced by the spectral difference,

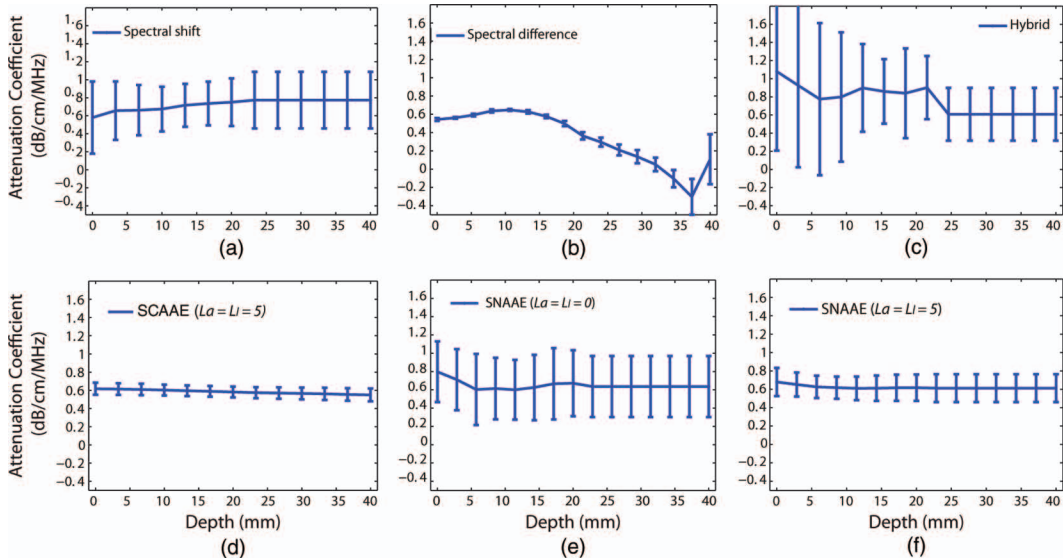


Fig. 11. Illustration of mean attenuation coefficient (AC) profiles generated by different methods for the tissue-mimicking phantom (TMP) data set B having AC 0.7 dB/cm/MHz. Mean profiles are estimated along width for AC maps shown in Figs. 9(i)–9(n) by different methods. Profiles are produced by the (a) spectral shift, (b) spectral difference, (c) hybrid, (d) spectral cross-correlation-based average attenuation estimation (SCAAE) (for  $L_a = L_l = 5$ ), (e) spectral normalization-based average attenuation estimation (SNAAE) (for  $L_a = L_l = 0$ ), and (f) SNAAE (for  $L_a = L_l = 5$ ) methods.



TABLE I. DATA SET C: ESTIMATED MEAN AC AND STD (IN PARENTHESES) BY THE PROPOSED AND OTHER TECHNIQUES AT THREE DIFFERENT ROIS.

Method	ROI X (dB/cm/MHz)	ROI Y (dB/cm/MHz)	ROI Z (dB/cm/MHz)
Spectral shift [16]	0.47 ( $\pm 0.09$ )	0.82 ( $\pm 0.71$ )	0.75 ( $\pm 0.12$ )
Spectral difference [19]	0.69 ( $\pm 0.41$ )	0.88 ( $\pm 0.69$ )	0.56 ( $\pm 0.19$ )
Hybrid [24]	0.59 ( $\pm 0.47$ )	0.84 ( $\pm 0.51$ )	0.57 ( $\pm 0.43$ )
SNAAE ( $L_a = L_l = 0$ )	0.60 ( $\pm 0.16$ )	0.22 ( $\pm 0.29$ )	0.49 ( $\pm 0.14$ )
SNAAE ( $L_a = L_l = 5$ )	0.48 ( $\pm 0.29$ )	1.00 ( $\pm 0.27$ )	0.51 ( $\pm 0.25$ )
SCAAE ( $L_a = L_l = 5$ )	0.54 ( $\pm 0.11$ )	0.91 ( $\pm 0.10$ )	0.48 ( $\pm 0.09$ )

True AC values: ROI X = 0.50, ROI Y = 0.95, ROI Z = 0.50 dB/cm/MHz.

hybrid, and spectral shift methods. In addition, to show the effectiveness of using the NN factor by the proposed SNAAE method, we present results for  $L_a = L_l = 0$  in Figs. 9(g) and 9(m). From Figs. 9(g) and 9(m), we see that the estimated AC values vary greatly even though the attenuation is uniform throughout the sample. The consistency and reliability of the estimates by the SNAAE and SCAAE methods with  $L_a = L_l = 5$  are thus well ensured as a result of incorporation of spectral-domain weighted nearest neighbors.

For better understanding of the estimation accuracy and consistency of the proposed methods, we plot the mean AC profiles for the AC maps generated by the proposed and other techniques in Figs. 10 and 11 for the TMP data sets A and B, respectively. From Figs. 10(a) and 11(a), we see that the means of the AC profiles produced by the spectral shift method are fairly close to the true values with moderate standard deviations (STDs), although they slightly vary near the transducer face, as shown in Fig. 10(a). The AC profiles produced by the spectral difference method have variation in the mean AC values along depth and deviate greatly from the true values [see Figs. 10(b) and 11(b)]. The hybrid method produces better AC profiles along the depth except near the transducer face, where higher STDs are also seen [see Figs. 10(c) and 11(c)]. The proposed SNAAE and SCAAE methods with

$L_a = L_l = 5$  produce AC profiles with almost accurate mean and lower STD, which indicate better consistency and accuracy of the estimation [see Figs. 10(d) and 10(f) and Figs. 11(d) and 11(f), respectively] than that of other techniques. Note that we have achieved better AC profiles without using a large spatial signal block averaging-based approach, using a cost function-based approach instead. To show the effectiveness of the NN factors, the AC profiles are produced by setting  $L_a = L_l = 0$  in the SNAAE method as shown in Figs. 10(e) and 11(e). We see from Figs. 10(e) and 10(f) and Figs. 11(e) and 11(f) that the STDs in the case of  $L_a = L_l = 0$  are higher than those in the  $L_a = L_l = 5$  case.

We now show the performance comparison of the proposed and other published techniques for a TMP having an inclusion with a different AC than that of the background. We use TMP data sets C and D for the purpose where data set B is used as the reference for both the sets. Three rectangular ROIs, X, Y, and Z, are selected for the AC estimation as shown in Fig. 12. Note that the ROIs X and Z are chosen from the background and the ROI Y is chosen from the lesion area. The estimated AC and STD values are shown in Tables I and II. We can see from these tables that the spectral shift method fails in estimating the mean AC values for the ROI Z in the data sets C (see Table I) and D (see Table II). The STD of the estimated value in the ROI Y is high for the data set C (see Table I). The spectral difference method also fails in estimating the mean AC value of the ROI X in the data set C (see Table I) and of the inclusion in the data set D, and the STD of the estimates is higher in all the cases (see Tables I and II). The hybrid method however, accurately estimates the mean AC values in all three ROIs for the data sets C and D (see Tables I and II), showing relatively better performance for the data set D. The STD of the estimates, however, is high for all the three ROIs in the data set C (see Table I). On the other hand, the estimated average AC values by the proposed SNAAE and SCAAE methods with  $L_a = L_l = 5$  are closer to the respective true values, with lower STDs. To show the effect of using the nearest neighbors, we set  $L_a = L_l = 0$  in the SNAAE method. From Tables I and II, we see that the mean AC estimates by the SNAAE method with  $L_a = L_l = 0$  varies greatly for the ROI Y in the data set C, and for the ROI Z in the data set D (see Tables I and II). Therefore, it appears that using spectral domain nearest neighbors is

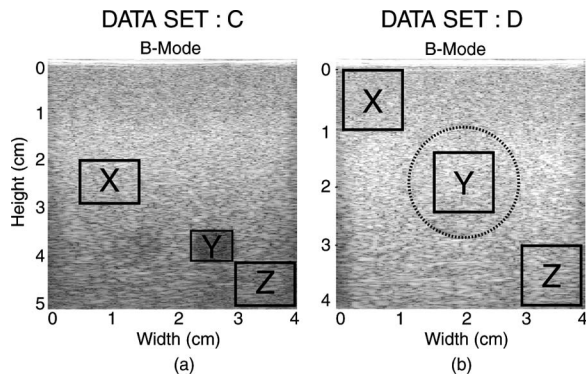


Fig. 12. B-mode images of the tissue-mimicking phantom (TMP) data sets C and D with inclusions. (a) Data set C contains a spherical inclusion of radius 0.35 cm, and attenuation coefficient (AC) 0.95 dB/cm/MHz. (b) Data set D contains a cylindrical inclusion of radius 0.835 cm, and AC 0.7 dB/cm/MHz. For both data sets, the AC of the background is 0.5 dB/cm/MHz. ROIs X, Y, and Z are of dimension 10  $\times$  10 mm each, except for the ROI Y of data set C, for which it is 7  $\times$  7 mm.

TABLE II. DATA SET D: ESTIMATED MEAN AC AND STD (IN BRACKET) BY THE PROPOSED AND OTHER TECHNIQUES AT THREE DIFFERENT ROIS.

Method	ROI X (dB/cm/MHz)	ROI Y (dB/cm/MHz)	ROI Z (dB/cm/MHz)
Spectral shift [16]	0.52 ( $\pm 0.05$ )	0.71 ( $\pm 0.15$ )	0.19 ( $\pm 0.19$ )
Spectral difference [19]	0.37 ( $\pm 0.60$ )	0.45 ( $\pm 0.47$ )	0.42 ( $\pm 0.36$ )
Hybrid [24]	0.51 ( $\pm 0.07$ )	0.70 ( $\pm 0.06$ )	0.51 ( $\pm 0.08$ )
SNAAE ( $L_a = L_l = 0$ )	0.53 ( $\pm 0.24$ )	0.72 ( $\pm 0.34$ )	0.30 ( $\pm 0.13$ )
SNAAE ( $L_a = L_l = 5$ )	0.52 ( $\pm 0.30$ )	0.71 ( $\pm 0.22$ )	0.50 ( $\pm 0.27$ )
SCAAE ( $L_a = L_l = 5$ )	0.49 ( $\pm 0.07$ )	0.73 ( $\pm 0.10$ )	0.49 ( $\pm 0.08$ )

True AC values: ROI X = 0.50, ROI Y = 0.70, ROI Z = 0.50 dB/cm/MHz.

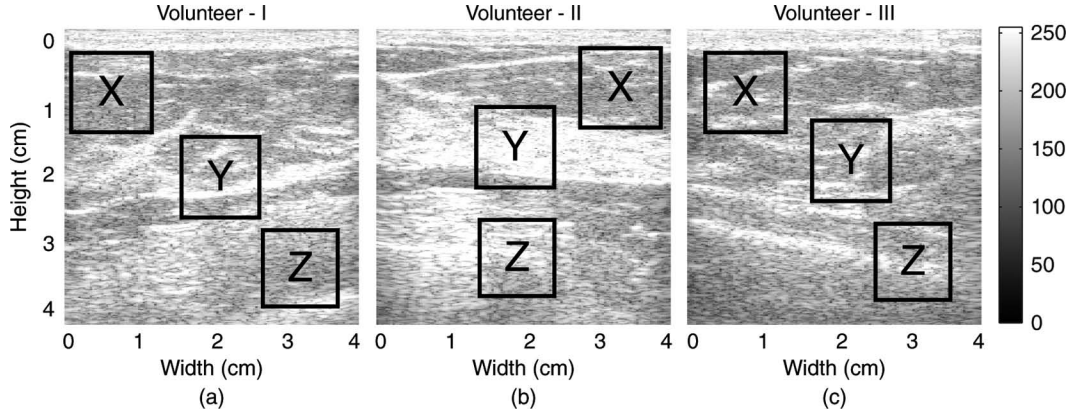


Fig. 13. B-mode images of the *in vivo* female breast data from (a) volunteer I, (b) volunteer II, and (c) volunteer III. These data correspond to arbitrary regions of normal breast tissues. ROIs X, Y, and Z are of dimension  $10 \times 10$  mm each.

effective in accurate AC estimation of a TMP with and without inclusions.

### B. In Vivo Breast Data Results

To show the efficacy of our proposed methods in practical applications, we estimate the AC of *in vivo* normal breast data that were acquired at BUET Medical Center, Dhaka, Bangladesh from three female volunteers (volunteer I, age: 48 years; volunteer II, age: 40 years; and volunteer III, age: 58 years) by using a SonixTOUCH Research (Ultrasonix Medical Corp.) scanner integrated with a L14-5/38 probe operating at 10 MHz and at a sampling rate

of 40 MHz. The fractional bandwidth of the transmitting RF pulse by the probe L14-5/38 is 65% at  $-6$ -dB spectral power level. An institutional review board (IRB) approved the study, and prior informed consent was taken from the volunteers for further use of these data in research. The data size was  $4 \times 4$  cm and the focus was set to 2 cm away from the transducer face. The ultrasound beam traverses through the skin, subcutaneous fat, superficial fascia, copper ligaments, glandular tissue, etc. The data pre-processing steps are described in the previous subsection. The B-mode images are shown in Fig. 13. During data acquisition, no TGC was used. The reported AC values of the soft biological and breast tissues are summarized in Table III.

To show the performance of the proposed and other published techniques for the *in vivo* normal female breast data, we use the TMP data set A as the reference for all three volunteers' data which are acquired with the same transducer and power settings as that of the data set A. Three rectangular ROIs X, Y, and Z are selected for the AC estimation as shown in Fig. 13. Note that the ROIs X and Z are chosen from the fatty tissue regions, whereas the ROI Y is chosen from the glandular tissue area. The estimated AC and STD values are shown in Tables IV, V, and VI for volunteers I, II, and III, respectively.

It is shown in Table III that the reported AC values of fatty tissue ranges from 0.35 to 0.60 dB/cm/MHz. We can see from the estimates of the ROIs X and Z (fatty region) in Tables IV, V, and VI that though the spectral shift

TABLE III. APPROXIMATE ATTENUATION COEFFICIENTS FOR SOFT BIOLOGICAL AND BREAST TISSUES.

Tissue type	Attenuation coefficient (dB/cm/MHz)	Source
Soft tissue	0.5–1.0	[37]
Soft tissue (Average)	0.60	[38]
Soft tissue (Average)	0.54	[39]
Fat	0.48	[39]
Fat	0.35	[8]
Fat	0.60	[38]
Fat	0.442	[40]
Breast (Average)	0.75	[39]
Glandular tissue	0.548	[40]
Fibrofatty parenchyma	0.98	[8]

TABLE IV. VOLUNTEER I: ESTIMATED MEAN AC AND STD (IN PARENTHESES) BY THE PROPOSED AND OTHER TECHNIQUES AT THREE DIFFERENT ROIS.

Method	ROI X (dB/cm/MHz)	ROI Y (dB/cm/MHz)	ROI Z (dB/cm/MHz)
Spectral shift [16]	0.34 ( $\pm 0.14$ )	0.85 ( $\pm 0.17$ )	0.35 ( $\pm 0.11$ )
Spectral difference [19]	0.63 ( $\pm 0.60$ )	0.97 ( $\pm 0.38$ )	0.25 ( $\pm 0.34$ )
Hybrid [24]	0.51 ( $\pm 0.08$ )	0.49 ( $\pm 0.07$ )	0.50 ( $\pm 0.07$ )
SNAAE ( $L_a = L_1 = 0$ )	0.51 ( $\pm 0.05$ )	0.40 ( $\pm 0.30$ )	0.61 ( $\pm 0.45$ )
SNAAE ( $L_a = L_1 = 5$ )	0.46 ( $\pm 0.23$ )	0.48 ( $\pm 0.26$ )	0.54 ( $\pm 0.31$ )
SCAAE ( $L_a = L_1 = 5$ )	0.43 ( $\pm 0.09$ )	0.52 ( $\pm 0.07$ )	0.48 ( $\pm 0.05$ )

method is successful in estimating the mean AC values closer to the reference range (i.e., 0.35 to 0.60 dB/cm/MHz) for volunteer I, it gives impractical estimates in the ROIs X and Z for volunteer II (see Table V), and in the ROI X for volunteer III (see Table VI). The spectral difference method gives AC estimates that deviate substantially from the reference range (i.e., 0.35 to 0.60 dB/cm/MHz) in most cases but gives reasonable AC estimates in the ROI X for volunteers I and III (see Tables IV, V, and VI). The hybrid method produces mean AC values in the range 0.48 to 0.51 dB/cm/MHz that are fairly inside the reference range (i.e., 0.35 to 0.60 dB/cm/MHz) with lower STDs for all three volunteers. From Tables IV, V, and VI, we see that the proposed SNAAE and SCAAE methods with  $L_a = L_1 = 5$  fairly estimate AC values with their means (i.e., 0.43 to 0.54 dB/cm/MHz) into the reference range (i.e., 0.35 to 0.60 dB/cm/MHz). In addition, the mean AC values estimated by the proposed SCAAE and SNAAE methods with  $L_a = L_1 = 5$  are close to each other, indicating the reliability of the estimation processes. On the other hand, for the glandular tissue (ROI Y in Tables IV, V, and VI), the spectral shift and spectral difference methods fail in estimating the mean AC values closer to the reference value (i.e., 0.548 dB/cm/MHz as shown in Table III); however, the hybrid method estimates mean AC values closer to the reported one (see Tables IV, V, and VI). The proposed SNAAE and SCAAE methods with  $L_a = L_1 = 5$  compute the AC values in the range 0.46 to 0.66 dB/cm/MHz and 0.50 to 0.56 dB/cm/MHz, respectively, that are reasonably closer to the reported value 0.548 dB/cm/MHz. The comparison with the reference AC value, however, would have been fair if more reported AC values were available for the glandular tissue. We also see that if nearest neighbors are not used (i.e.,  $L_a = L_1 = 0$ ), then the SNAAE estimates (see Tables IV, V,

and VI) deviate widely from the corresponding reported values, which emphasizes the importance of the NN concept introduced in this paper. Overall, it can be said that the hybrid, proposed SNAAE and SCAAE (with  $L_a = L_1 = 5$ ) methods estimate AC values reasonably consistent with the reported values shown in Table III. However, the hybrid (and also the spectral shift and spectral difference) method uses large spatial signal blocks in generating stable power spectra in contrast to the proposed methods, for which nearest neighbors are used in estimating consistent AC values in an elegant way. Calculating the AC of pathologic breast tissue using the methods that use large spatial signal blocks might not be practical, whereas the proposed methods significantly overcome this limitation. Therefore, it can be said from the practical point of view that the proposed SNAAE and SCAAE methods using the weighted nearest neighbors are more suitable in AC estimation for *in vivo* breast data.

#### IV. CONCLUSIONS

This paper has introduced two novel methods for spectral domain ultrasonic attenuation estimation of soft tissues using exponentially weighted nearest neighbors. Assuming that the AC is essentially identical in a small tissue region and a continuous function among neighborhoods, we have estimated AC with improved consistency and accuracy from the slope of the regression line fitted to the modified average midband fit value and also from the average center frequency shift along the depth using the proposed SNAAE and SCAAE methods, respectively. The average midband fit value is obtained from an average regression line computed from the exponentially weighted neighboring window regression lines, in both the axial

TABLE V. VOLUNTEER II: ESTIMATED MEAN AC AND STD (IN PARENTHESES) BY THE PROPOSED AND OTHER TECHNIQUES AT THREE DIFFERENT ROIS.

Method	ROI X (dB/cm/MHz)	ROI Y (dB/cm/MHz)	ROI Z (dB/cm/MHz)
Spectral shift [16]	—*	0.31 ( $\pm 0.09$ )	0.09 ( $\pm 0.11$ )
Spectral difference [19]	0.23 ( $\pm 0.50$ )	0.79 ( $\pm 0.53$ )	0.23 ( $\pm 0.41$ )
Hybrid [24]	0.48 ( $\pm 0.08$ )	0.49 ( $\pm 0.05$ )	0.48 ( $\pm 0.07$ )
SNAAE ( $L_a = L_1 = 0$ )	0.31 ( $\pm 0.27$ )	0.66 ( $\pm 0.31$ )	0.24 ( $\pm 0.26$ )
SNAAE ( $L_a = L_1 = 5$ )	0.43 ( $\pm 0.36$ )	0.46 ( $\pm 0.26$ )	0.46 ( $\pm 0.18$ )
SCAAE ( $L_a = L_1 = 5$ )	0.43 ( $\pm 0.06$ )	0.50 ( $\pm 0.05$ )	0.52 ( $\pm 0.10$ )

\*Negative estimate.

TABLE VI. VOLUNTEER III: ESTIMATED MEAN AC AND STD (IN PARENTHESES) BY THE PROPOSED AND OTHER TECHNIQUES AT THREE DIFFERENT ROIS.

Method	ROI X (dB/cm/MHz)	ROI Y (dB/cm/MHz)	ROI Z (dB/cm/MHz)
Spectral shift [16]	—*	0.86 ( $\pm 0.10$ )	0.54 ( $\pm 0.18$ )
Spectral difference [19]	0.56 ( $\pm 0.48$ )	0.72 ( $\pm 0.50$ )	0.21 ( $\pm 0.34$ )
Hybrid [24]	0.48 ( $\pm 0.07$ )	0.52 ( $\pm 0.06$ )	0.51 ( $\pm 0.05$ )
SNAAE ( $L_a = L_l = 0$ )	0.47 ( $\pm 0.27$ )	0.21 ( $\pm 0.14$ )	0.58 ( $\pm 0.22$ )
SNAAE ( $L_a = L_l = 5$ )	0.43 ( $\pm 0.17$ )	0.66 ( $\pm 0.33$ )	0.49 ( $\pm 0.20$ )
SCAAE ( $L_a = L_l = 5$ )	0.45 ( $\pm 0.03$ )	0.56 ( $\pm 0.15$ )	0.43 ( $\pm 0.07$ )

\*Negative estimate.

and lateral directions, and the average center frequency downshift is computed from the maximization of a cost function defined from the NSCC of exponentially weighted nearest neighbors in both directions. Unlike the conventional approaches, the proposed methods with weighted nearest neighbors allow us to estimate the AC values for each of the scan-lines independently, which in turn helps us to formulate a built-in averaging technique in the spectral domain. The estimated AC values of our experimental tests using the TMP have demonstrated better consistency and reliability of our proposed methods over the other reported techniques. In addition, for the *in vivo* normal breast data, the estimated AC values by our methods have been found to be consistent with the AC values reported in the literature. Further investigations are underway for determining the effectiveness of the methods for computing ACs of *in vivo* data of patients with breast lesions.

## ACKNOWLEDGMENT

The *in vivo* breast data were acquired in BUET Medical Center by Dr. F. Alam, Medical Officer, Department of Radiology and Imaging, Bangabandhu Sheikh Mujib Medical University, Dhaka, Bangladesh.

## REFERENCES

- [1] K. A. Dines and A. C. Kak, "Ultrasonic attenuation tomography of soft tissues," *Ultrason. Imaging*, vol. 1, no. 1, pp. 16–33, 1979.
- [2] G. Berger, P. Laugier, M. Fink, and J. Perrin, "Optimal precision in ultrasound attenuation estimation and application to the detection of Duchenne muscular dystrophy carriers," *Ultrason. Imaging*, vol. 9, no. 1, pp. 1–17, 1987.
- [3] B. J. Oosterveld, J. M. Thijssen, P. C. Hartman, R. L. Romijn, and G. J. Rosenbusch, "Ultrasound attenuation and texture analysis of diffuse liver disease: Methods and preliminary results," *Phys. Med. Biol.*, vol. 36, no. 8, pp. 1039–1064, 1991.
- [4] T. Wilson, Q. Chen, J. A. Zagzebski, T. Varghese, and L. Van-Middlesworth, "Initial clinical experience imaging scatterer size and strain in thyroid nodules," *J. Ultrasound Med.*, vol. 25, no. 8, pp. 1021–1029, 2006.
- [5] P. D. Lui, M. K. Terris, J. E. McNeal, and T. A. Stamey, "Prostate cancer: Indications for ultrasound guided transition zone biopsies in the detection of prostate cancer," *J. Urol.*, vol. 153, no. 3, pt. 2, pp. 1000–1003, 1995.
- [6] G. Berger, P. Laugier, J. C. Thalabard, and J. Perrin, "Global breast attenuation: Control group and benign breast diseases," *Ultrason. Imaging*, vol. 12, no. 1, pp. 47–57, 1990.
- [7] L. Landini, R. Sarnelli, and F. Squartini, "Frequency-dependent attenuation in breast tissue characterization," *Ultrasound Med. Biol.*, vol. 11, no. 4, pp. 599–603, 1985.
- [8] L. Landini and R. Sarnelli, "Evaluation of the attenuation coefficients in normal and pathological breast tissue," *Med. Biol. Eng. Comput.*, vol. 24, no. 3, pp. 243–247, 1986.
- [9] S. W. Flax, N. J. Pelc, G. H. Glover, F. D. Gutmann, and M. McLachlan, "Spectral characterization and attenuation measurements in ultrasound," *Ultrason. Imaging*, vol. 5, no. 2, pp. 95–116, 1983.
- [10] H. S. Jang, T. K. Song, and S. B. Park, "Ultrasound attenuation estimation in soft tissue using the entropy difference of pulsed echoes between two adjacent envelope segments," *Ultrason. Imaging*, vol. 10, no. 4, pp. 248–264, 1988.
- [11] B. S. Knipp, J. A. Zagzebski, T. A. Wilson, F. Dong, and E. L. Madsen, "Attenuation and backscatter estimation using video signal analysis applied to B-mode images," *Ultrason. Imaging*, vol. 19, no. 3, pp. 221–233, 1997.
- [12] R. Kuc, "Bounds on estimating the acoustic attenuation of small tissue regions from reflected ultrasound," *Proc. IEEE*, vol. 73, no. 7, pp. 1159–1168, 1985.
- [13] K. J. Parker and R. C. Waag, "Measurement of ultrasonic attenuation within regions selected from B-scan images," *IEEE Trans. Biomed. Eng.*, vol. 30, no. 8, pp. 431–437, 1983.
- [14] S. Leeman, L. Ferrari, J. P. Jones, and M. Fink, "Perspectives on attenuation estimation from pulse-echo signals," *IEEE Trans. Sonics Ultrason.*, vol. 31, no. 4, pp. 352–361, 1984.
- [15] P. A. Narayana and J. Ophir, "The measurement of attenuation in nonlinearly attenuating media by the zero crossing method," *Ultrasound Med. Biol.*, vol. 10, no. 6, pp. 715–718, 1984.
- [16] H. Kim and T. Varghese, "Attenuation estimation using spectral cross-correlation," *IEEE Trans. Ultrason. Ferroelectr. Freq. Control*, vol. 54, no. 3, pp. 510–519, 2007.
- [17] T. A. Bigelow and W. D. O'Brien Jr., "Impact of local attenuation approximations when estimating correlation length from backscattered ultrasound echoes," *J. Acoust. Soc. Am.*, vol. 120, no. 1, pp. 546–553, 2006.
- [18] K. J. Parker, R. M. Lerner, and R. C. Waag, "Comparison of techniques for in vivo attenuation measurements," *IEEE Trans. Biomed. Eng.*, vol. 35, no. 12, pp. 1064–1068, 1988.
- [19] L. X. Yao, J. A. Zagzebski, and E. L. Madsen, "Backscatter coefficient measurements using a reference phantom to extract depth-dependent instrumentation factors," *Ultrason. Imaging*, vol. 12, no. 1, pp. 58–70, 1990.
- [20] R. Kuc, "Clinical application of an ultrasound attenuation coefficient estimation technique for liver pathology characterization," *IEEE Trans. Biomed. Eng.*, vol. 27, no. 6, pp. 312–319, 1980.
- [21] R. Kuc, "Estimating acoustic attenuation from reflected ultrasound signals: Comparison of spectral-shift and spectral-difference approaches," *IEEE Trans. Acoust. Speech Signal Process.*, vol. 32, no. 1, pp. 1–6, 1984.
- [22] R. Kuc and M. Schwartz, "Estimating the acoustic attenuation coefficient slope for liver from reflected ultrasound signals," *IEEE Trans. Sonics Ultrason.*, vol. 26, no. 5, pp. 353–361, 1979.
- [23] M. Insana, J. Zagzebski, and E. Madsen, "Improvements in the spectral difference method for measuring ultrasonic attenuation," *Ultrason. Imaging*, vol. 5, no. 4, pp. 331–345, 1983.
- [24] H. Kim and T. Varghese, "Hybrid spectral domain method for attenuation slope estimation," *Ultrasound Med. Biol.*, vol. 34, no. 11, pp. 1808–1819, 2008.



- [25] K. Schmidt, G. Mies, and L. Sokoloff, "Model of kinetic behavior of deoxyglucose in heterogeneous tissues in brain: A reinterpretation of the significance of parameters fitted to homogeneous tissue models," *J. Cereb. Blood Flow Metab.*, vol. 11, no. 1, pp. 10–24, 1991.
- [26] Y. Labyed and T. A. Bigelow, "A theoretical comparison of attenuation measurement techniques from backscattered ultrasound echoes," *J. Acoust. Soc. Am.*, vol. 129, no. 4, pp. 2316–2324, 2011.
- [27] M. A. Fink and J. F. Cardoso, "Diffraction effects in pulse-echo measurement," *IEEE Trans. Sonics Ultrason.*, vol. 31, no. 4, pp. 313–329, 1984.
- [28] P. He, "Acoustic attenuation estimation for soft tissue from ultrasound echo envelope peaks," *IEEE Trans. Ultrason. Ferroelectr. Freq. Control*, vol. 36, no. 2, pp. 197–203, 1989.
- [29] P. M. Shankar, "A general statistical model for ultrasonic backscattering from tissues," *IEEE Trans. Ultrason. Ferroelectr. Freq. Control*, vol. 47, no. 3, pp. 727–736, 2000.
- [30] G. Treece, R. Prager, and A. Gee, "Ultrasound attenuation measurement in the presence of scatter variation for reduction of shadowing and enhancement," *IEEE Trans. Ultrason. Ferroelectr. Freq. Control*, vol. 52, no. 12, pp. 2346–2360, 2005.
- [31] F. L. Lizzi, M. Greenebaum, E. J. Feleppa, M. Elbaum, and D. J. Coleman, "Theoretical frame work for spectrum analysis in ultrasonic tissue characterization," *J. Acoust. Soc. Am.*, vol. 73, no. 4, pp. 1366–1373, 1983.
- [32] S. K. Alam, E. J. Feleppa, M. Rondeau, A. Kalisz, and B. S. Garra, "Ultrasonic multi-feature analysis procedure for computer-aided diagnosis of solid breast lesions," *Ultrason. Imaging*, vol. 33, no. 1, pp. 17–38, 2011.
- [33] J. C. Bamber, F. A. Duck, A. C. Baker, and H. C. Starritt, "Ultrasonic properties of tissues," in *Ultrasound in Medicine*, Eds., Bristol, England: Institute of Physics, 1998, ch. 4, pp. 57–88.
- [34] Y. Fujii, N. Taniguchi, K. Itoh, K. Shigeta, Y. Wang, and J. Tsao, "A new method for attenuation coefficient measurement in the liver," *J. Ultrasound Med.*, vol. 21, pp. 783–788, 2002.
- [35] B. Pan, K. Qian, H. Xie, and A. Asundi, "Two-dimensional digital image correlation for in-plane displacement and strain measurement: A review," *Meas. Sci. Technol.*, vol. 20, art. no. 062001, 2009.
- [36] P. Welch, "The use of fast Fourier transform for the estimation of power spectra: A method based on time averaging over short, modified periodograms," *IEEE Trans. Audio Electroacoust.*, vol. 15, no. 2, pp. 70–73, 1967.
- [37] T. Baldewick, P. Laugier, A. Herment, and G. Berger, "Application of autoregressive spectral analysis for ultrasound attenuation estimation: Interest in highly attenuating medium," *IEEE Trans. Ultrason. Ferroelectr. Freq. Control*, vol. 42, no. 1, pp. 99–109, 1995.
- [38] P. N. T. Wells, "Ultrasonic imaging of the human body," *Rep. Prog. Phys.*, vol. 62, pp. 671–722, 1999.
- [39] M. O. Culjat, D. Goldenberg, P. Tewari, and R. S. Singh, "A review of tissue substitutes for ultrasound imaging," *Ultrasound Med. Biol.*, vol. 36, no. 6, pp. 861–873, 2010.
- [40] S. Huang and P. Li, "Ultrasonic computed tomography reconstruction of the attenuation coefficient using a linear array," *IEEE Trans. Ultrason. Ferroelectr. Freq. Control*, vol. 52, no. 11, pp. 2011–2022, 2005.



**Md. Kamrul Hasan** received the B.Sc. and M. Sc. degrees in electrical and electronic engineering from the Bangladesh University of Engineering and Technology (BUET), Dhaka, Bangladesh, in 1989 and 1991, respectively. He received his M.Eng. and Ph.D. degrees in information and computer sciences from Chiba University, Japan, in 1995 and 1997, respectively. In 1989, he joined BUET as a Lecturer in the Department of Electrical and Electronic Engineering. He is currently working as a Professor in the same department.

He was a postdoctoral fellow and research associate at Chiba University, Japan, and Imperial College, London, respectively. He worked as a short-term invited research fellow at the University of Tokyo, Japan, and Professor of International Scholars of Kyung Hee University, Korea.

His current research interests are in digital signal processing, adaptive filtering, speech and image processing, and medical imaging. He has authored or coauthored more than 100 scientific publications.

He is currently serving as an associate editor for *IEEE Access*.



**Mohammad Arafat Hussain** was born in Bangladesh in 1988. He received the B.Sc. degree in electrical and electronic engineering from the Bangladesh University of Engineering and Technology (BUET), Dhaka, Bangladesh, in 2011.

He worked as a software engineer at the Samsung Bangladesh R&D Center from March to June, 2011. He is currently a research engineer at DSP Research Lab, BUET, working on ultrasonic elasticity imaging and attenuation estimation. His research interests include ultrasonic imaging and tissue characterization.



**Sharmin R. Ara** was born in Bangladesh in 1974. She received the B.Sc. degree in electrical and electronic engineering from the Bangladesh University of Engineering and Technology (BUET), Dhaka, Bangladesh, and the M.Sc. degree in electrical and computer engineering from Southern Illinois University, in 2000 and 2007, respectively. She is currently working toward her Ph.D. degree in the Department of Electrical and Electronic Engineering at BUET.

She is currently a Senior Lecturer in the Department of Electrical and Electronic Engineering at East West University, Bangladesh. Her research interests include ultrasonic imaging and tissue characterization.



**Soo Yeol Lee** received the M.S. and Ph.D. degrees in electronic engineering from the Korea Advanced Institute of Science and Technology (KAIST), Seoul, South Korea, in 1985 and 1989, respectively. He was with Department of Biomedical Engineering in Konkuk University, South Korea, from 1992 to 1999. In 1999, he joined the Department of Biomedical Engineering at Kyung Hee University, South Korea, where he is the director of the functional and metabolic imaging research center (FMIC). His research interests are MRI, CT, elastography, and medical image processing.



**Sheikh Kaiser Alam** was born in Bangladesh. He received the Bachelor of Technology (Honors) degree in electronics and electrical communication engineering from the Indian Institute of Technology, Kharagpur, India in 1986, and the M.S. and Ph.D. degrees in electrical engineering from the University of Rochester, Rochester, NY, in 1991 and 1996, respectively.

Dr. Alam was a lecturer in the Department of Electrical and Electronic Engineering at the Bangladesh Institute of Technology, Rajshahi, Bangladesh, from 1986 to 1989. While pursuing graduate studies at the University of Rochester, his work on improving the ultrasonic estimation of blood velocity led to a patented technique for ultrasonic blood flow imaging. As a postdoctoral fellow at the University of Texas Medical School at Houston from 1995 to 1998, he worked on elastography, a new ultrasonic imaging modality to image elastic properties of tissue. Dr. Alam has been a Member of the Research Staff at Riverside Research Institute in New York since 1998, where he has been working on a variety of research topics in biomedical imaging. Since 2010, he has been a visiting faculty member in the Department of Electrical and Electronic Engineering at the Islamic University of Technology, Gazipur, Bangladesh. His research interests include diagnostic and therapeutic applications of ultrasound and optics, and signal/image processing with applications to medical imaging.

Dr. Alam has written more than 30 papers in international journals and holds several patents. He is a member of Sigma Xi, the Acoustical Society of America (ASA), and the Society of Photographic Instrumentation Engineers (SPIE), and a Senior Member of the American Institute of Ultrasound in Medicine (AIUM) and IEEE. Dr. Alam is a member of the editorial board of *Ultrasonic Imaging* and the *Journal of Medical Engineering*. He was a recipient of the prestigious Fulbright Scholar Award in 2011–2012.